A NEW MICRO-SEISMIC MODEL FOR FAULT RECONSTRUCTION IN REISSNER-MINDLIN PLATES

A.A.M. DA SILVA AND A.A. NOVOTNY

Abstract. In this work, a new micro-seismic opening model for the fault reconstruction in Reissner-Mindlin plates is proposed. The description of micro-seismic faults is given by a combination of dipoles specified in terms of the seismic moment tensor. In particular, we are interested in the spatial reconstruction and characterization of micro-seismic events in plate structures via joint source location and moment tensor inversion from pointwise measurements of the plate displacement field. The basic idea consists in minimizing a functional measuring the misfit between observed and predicted data with respect to a set of admissible solutions, leading to a non-iterative second order reconstruction algorithm. As a result, the reconstruction process becomes very robust with respect to noisy data and independent of any initial guess. Finally, a set of numerical experiments is presented, showing the efficiency of the methodology in the reconstruction of four simultaneous faults, by considering varying configurations of three as well as uni-axial sensors in the presence and absence of noisy data.

1. Introduction

Faults identification process in their initial stage has great importance in many physical and engineering problems. The available methods for fault identification based on dynamic tests are usually classified into four categories: time-domain methods, frequency-domain methods, methods based on impedance, and modal analysis. Important contributions to the faults detection procedure have been reported in the literature [1, 2, 3, 4, 5, 6, 7, 8, 9, 10, 11, 12, 13, 14]. Besides, in [15] the methods for fault identification are classified in the following levels: detection of the presence of damage in the structure (level 1), location of the region affected by the fault (level 2), quantitative information (size) of the faults (level 3) and indication about the safety of the structure and the prediction of its remaining lifetime (level 4). See, for instance, the paper [16] dealing with detection and location of damages in plate structures (level 1 and level 2) by using the topological derivative method. See also the paper [17] in which a novel full-waveform technique is proposed for the spatial reconstruction and characterization of micro-faults events via joint source location and moment tensor inversion (levels 1-3). Inspired on the topological derivative method, in the present work we propose a new micro-seismic opening model for the fault reconstruction in Reissner-Mindlin plates.

The topological derivative has been specifically conceived to provide a precise information on the sensitivity of a given shape functional with respect to topological domain perturbations [18]. The origin of the topological derivative method in optimal design can be dated to the work by Schumacher [19] on the optimal location of holes within elastic structures. The first mathematical justifications for topological derivatives in the framework of partial differential equations are due to Sokołowski and Żochowski [20] and Garreau at al. [21], in the context of the Poisson equation and the Navier system for Neumann and Dirichlet holes. Therefore, this relatively new concept in shape optimization has applications in many different fields such as shape and topology optimization, geometrical inverse problems, image processing, multi-scale

Key words and phrases. Micro-seismic moment tensor inversion, topological derivative method, Reissner-Mindlin plate model.

material design and mechanical modelling, including damage and fracture evolution phenomena. See, for instance, the special issue on the topological derivative method and its applications in computational engineering recently published in the Engineering Computations Journal [22], covering various topics ranging from new theoretical developments [23, 24, 25] to applications in structural and fluid dynamics topology optimization [26, 27, 28], geometrical inverse problems [29, 30, 31, 32, 33] synthesis and optimal design of metamaterials [34, 35], fracture mechanics modelling [36], up to industrial applications [37] and experimental validation of the topological derivative method [38].

Seismic and micro-seismic source characterization is an important area of research in geophysics, engineering, and materials science due to its central role in the understanding of earthquake and faulting processes [39], for instance. Small sudden material failures can be represented by a linear combination of force dipoles describing micro-seismic sources [40]. In this setting, the nature of the micro-fault is completely characterized by the seismic moment tensor [41]. This theory is therefore helpful for investigating the failure of brittle materials in general, with applications in the monitoring of mines, highway bridges, offshore platforms and fracking process.

In this paper, we are interested in the delamination process represented by a micro-fault lying in the middle plane of a plate structure, orthogonal to its cross-section. The forward problem is governed by the elastodynamic Reissner-Mindlin plate bending problem in the frequency domain. The description of micro-seismic faults is given by a combination of dipoles specified in terms of the seismic moment tensor. The basic idea consists in minimizing a functional measuring the misfit between observed and predicted data with respect to a set of admissible micro-seismic sources by using the topological derivative method. In order to test the efficiency of the proposed methodology, a set of numerical experiments dealing with the reconstruction of four simultaneous faults are presented by considering varying configurations of three as well as uni-axial sensors in the presence and absence of noisy data.

The paper is organized as follows. In Section 2, a novel micro-fault opening model for Reissner-Mindlin plate model is derived. The seismic moment tensor inversion theory is introduced in Section 3. In Section 4, the sensitivity analysis of the tracking-type functional with respect to source perturbations living in the set of admissible solutions is presented. The resulting initial-guess free and non-iterative reconstruction algorithm is described in Section 5. Some numerical experiments are presented in Section 6, showing different features of the reconstruction algorithm. Finally, the paper ends with some concluding remarks in Section 7.

2. Micro-fault opening model

Let us consider an open and bounded domain $D \subset \mathbb{R}^3$, such that one dimension is much smaller than the other two dimensions. The flat domain D is described as follows

$$D = \{(x, z)^\top \in \mathbb{R}^2 \times \mathbb{R} : -h/2 < z < +h/2\}, \tag{2.1}$$

where h is the plate thickness. The middle plane of the plate is then represented by $\Omega \subset \mathbb{R}^2$, such that $D = \Omega \times (-h/2, +h/2)$. We assume that there is a micro-fault Ξ lying in the middle plane Ω of the plate structure, as sketch in Figure 1.

According to [40], the micro-fault can be characterized by a dipole of the form

$$F(\xi) = M \nabla_{\xi^*} \delta(\xi - \xi^*), \tag{2.2}$$

where $\delta(\xi-\xi^*)$ is the three-dimensional Dirac function with pole at ξ^*, with $\xi=(\xi_1,\xi_2,\xi_3)^\top$. Its gradient with respect to ξ^* has to be understood in the following sense

$$\begin{aligned}\nabla_{\xi^*}\delta(\xi-\xi^*) = &\frac{\partial}{\partial\xi_1^*}\delta(\xi_1-\xi_1^*)\delta(\xi_2-\xi_2^*)\delta(\xi_3-\xi_3^*)e_1\\ &+\delta(\xi_1-\xi_1^*)\frac{\partial}{\partial\xi_2^*}\delta(\xi_2-\xi_2^*)\delta(\xi_3-\xi_3^*)e_2\\ &+\delta(\xi_1-\xi_1^*)\delta(\xi_2-\xi_2^*)\frac{\partial}{\partial\xi_3^*}\delta(\xi_3-\xi_3^*)e_3,\end{aligned}\tag{2.3}$$

with e_i, $i=1,2,3$, used to denote the canonical basis of the three-dimensional Euclidean space $\mathbb{R}^3$. By introducing the notation $\xi=(x,z)^\top$, with $x=(\xi_1,\xi_2)^\top$ and $z=\xi_3$, we have

$$\nabla_{\xi^*}\delta(\xi-\xi^*)=\begin{pmatrix}\nabla_{x^*}\delta(x-x^*)\delta(z-z^*)\\ \delta(x-x^*)\frac{\partial}{\partial z^*}\delta(z-z^*)\end{pmatrix}.\tag{2.4}$$

The seismic moment tensor M is defined as

$$M=a_\Xi\lambda[\![u]\!]\cdot n\,\mathrm{I}_3+a_\Xi\mu(n\otimes[\![u]\!]+[\![u]\!]\otimes n),\tag{2.5}$$

where a_Ξ is the area of a newly created micro-fault Ξ giving rise to the acoustic emission, n is the unit normal vector to the micro-fault surface, $[\![u]\!]$ is the average displacement jump across the micro-fault, (μ,λ) are the Lamé coefficients and I_3 is the three dimensional identity tensor.

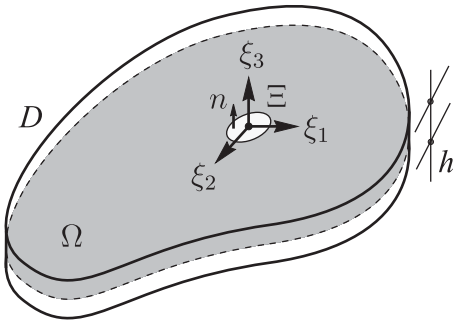

FIGURE 1. Flat domain D with a micro-fault Ξ surface lying in the middle plane Ω of the plate structure with thickness h. The unit normal vector n is perpendicular to the micro-fault surface Ξ. The three-dimensional Cartesian coordinate system is denoted by ξ_1, ξ_2 and ξ_3.

The Reissner-Mindlin plate bending problem, we are dealing with, is based on the kinematic assumption that the normal fibers to the middle plane of the plate remain straight during the deformation process and do not suffer variations in their length, but they do not necessarily remain normal to the middle plane. Consequently, the transverse shear deformation are not negligible and the normal deformation is null. Therefore, the plate displacement $u: D\to\mathbb{C}^3$ can be decomposed as $u(x,z)=(-z\theta(x),w(x))^\top$, where $\theta:\Omega\to\mathbb{C}^2$ is the rotation vector field and $w:\Omega\to\mathbb{C}$ is the transverse displacement.

In this paper, we are interested in the delamination process represented by the micro-fault Ξ lying in the middle plane Ω, orthogonal to the plate cross section, which is one of the most important fail mechanism of composite plate structures[1]. Therefore, the normal in (2.5) is given by $n=(0,1)^\top\in\mathbb{R}^2\times\mathbb{R}$ and the pole $z^*=0$, as shown in Figure 1. We assume that

[1]Note however that fault mechanisms in plates are much more complicated phenomena usually occurring far from the middle plane of the plate where the stresses are higher.

the micro-fault may open in traction, so that $[\![u]\!] = (0, [\![w]\!])^\top$. From these elements, in our simplified setting the seismic moment tensor is given by

$$M = \begin{pmatrix} \alpha\,\mathrm{I} & 0 \\ 0 & \beta \end{pmatrix}, \tag{2.6}$$

where I is the two-dimensional identity tensor. The entries α and β are defined as

$$\alpha = a_\Xi [\![w]\!] \lambda \qquad \text{and} \qquad \beta = a_\Xi [\![w]\!] (2\mu + \lambda). \tag{2.7}$$

By setting $z^* = 0$, integration over the plate thickness yields

$$\int_{-\frac{h}{2}}^{+\frac{h}{2}} \begin{pmatrix} \alpha\,\mathrm{I} & 0 \\ 0 & \beta \end{pmatrix} \begin{pmatrix} \nabla_{x^*}\delta(x-x^*)\delta(z-z^*) \\ \delta(x-x^*)\frac{\partial}{\partial z^*}\delta(z-z^*) \end{pmatrix}_{|_{z^*=0}} dz = \begin{pmatrix} \alpha \nabla_{x^*}\delta(x-x^*) \\ 0 \end{pmatrix}, \tag{2.8}$$

where we have used the following identities

$$\int_{-\frac{h}{2}}^{\frac{h}{2}} \delta(z-z^*)_{|_{z^*=0}} dz = 1, \quad \int_{-\frac{h}{2}}^{\frac{h}{2}} \frac{\partial}{\partial z^*}\delta(z-z^*)_{|_{z^*=0}} dz = 0. \tag{2.9}$$

Note that this result would be expected in the context of Reissner-Mindlin plate theory since the normal deformation is null. In addition, the normal to the micro-fault surface is fixed (assumed to be known) and points toward the orthogonal direction to the middle plane Ω of the plate. In this way, the traction mode is completely characterized by α. In particular, once α is found, parameter β can be promptly obtained as

$$\beta = \alpha \frac{2\mu + \lambda}{\lambda}. \tag{2.10}$$

Therefore, we have to keep in mind that our model is able to handle micro-faults lying in the middle plane of the plate under opening mechanism in traction, only. On the other hand, it is also worth to stress that delamination process in plates is a three-dimensional phenomenon occurring not only in traction and not necessarily in the middle plane of the plate, as postulated here. However, we believe that these more complicated phenomena can be better modelled by considering higher-order plate theory following similar reasoning as presented in this section.

3. Seismic moment tensor inversion

The transverse displacement and rotations of the plate in the time harmonic regime written in the frequency domain is governed by the following system of partial differential equations: Find (θ, w), such that

$$\left\{ \begin{array}{rcl} -\mathrm{div}\mathcal{M}(\theta) + \mathcal{Q}(\theta, w) - k_b^2\theta &=& f, \\ \\ \mathrm{div}\mathcal{Q}(\theta, w) - k_s^2 w &=& 0, \end{array} \right. \tag{3.1}$$

where $k_b \in \mathbb{R}$ and $k_s \in \mathbb{R}$ are the bending and shear wave numbers given by

$$k_b^2 = \frac{h^3}{12}\rho\omega^2 \quad \text{and} \quad k_s^2 = h\rho\omega^2, \tag{3.2}$$

with ρ the density and ω the frequency of wave motion. The source term $f \in C_\delta(\Omega)$ is given by a superposition of a number N of dipoles characterized by the two-dimensional Dirac delta function $\delta(x - x_i)$ and by the seismic moment tensor with entries $\alpha_i \in \mathbb{C}$, for $i = 1, \cdots, N$. Therefore, the set of admissible micro-seismic sources $C_\delta(\Omega)$ is defined as

$$C_\delta(\Omega) := \{ f : \Omega \to \mathbb{C}^2 \,|\, f(x) = \sum_{i=1}^{N} \alpha_i \nabla_{x_i}\delta(x - x_i) \}. \tag{3.3}$$

The system (3.1) is endowed with the essential boundary condition $w = 0$ on $\partial\Omega$, so that the plate is assumed to be simply supported, but without loss of generality. In addition, $\mathcal{M}(\theta)$ is the generalized bending moment tensor given by

$$\begin{aligned}\mathcal{M}(\theta) &= \frac{Eh^3}{12(1-\nu^2)}[(1-\nu)\mathbb{I} + \nu \mathrm{I} \otimes \mathrm{I}](\nabla\theta)^s \\ &= \frac{Eh^3}{12(1-\nu^2)}[(1-\nu)(\nabla\theta)^s + \nu \mathrm{div}(\theta)\mathrm{I}] \end{aligned} \tag{3.4}$$

and $\mathcal{Q}(\theta, w)$ is the generalized shear tensor, namely

$$\mathcal{Q}(\theta, w) = \frac{5Eh}{12(1+\nu)}(\theta - \nabla w), \tag{3.5}$$

with I and $\mathbb{I}$ used to denote the second and fourth order identity tensors, respectively, whereas E is the Young modulus and ν is the Poisson ratio. Some terms in the above equations still require explanation. Using the Einstein summation convention over repeated indices i, j, k, l, we specifically have $\mathrm{I} = \delta_{ij} e_i \otimes e_j$ and $\mathbb{I} = \frac{1}{2}(\delta_{ik}\delta_{jl} + \delta_{il}\delta_{jk}) e_i \otimes e_j \otimes e_k \otimes e_l$, where δ_{ij} is the Kronecker delta. In addition, $(\nabla\theta)^s$ is used to denote the symmetric part of the gradient of the vector function θ, namely $(\nabla\theta)^s = \frac{1}{2}(\nabla\theta + (\nabla\theta)^\top)$. Finally, $\mathrm{div}(\theta) = \mathrm{I} \cdot \nabla\theta = \mathrm{trace}(\nabla\theta)$.

The seismic moment tensor inversion, we are dealing with, consists in reconstructing the source $f^* \in C_\delta(\Omega)$ from pointwise domain measurement of the plate displacement field (θ^*, w^*). More precisely, we want to minimize in the set of admissible micro-seismic sources $C_\delta(\Omega)$ a functional measuring the misfit between the available data (measurement) and the solution computed from the model problem, namely

$$\underset{f \in C_\delta(\Omega)}{\text{Minimize}}\ \mathcal{J}(w, \theta). \tag{3.6}$$

The misfit functional $\mathcal{J}(w, \theta)$ is defined as

$$\mathcal{J}(w, \theta) = \frac{1}{2} \sum_{\ell=1}^{N_s} \int_\Omega (|w - w^*|^2 + \|\theta - \theta^*\|^2) \delta(x - x_\ell)\, dx, \tag{3.7}$$

where (w, θ) is the solution to (3.1), (w^*, θ^*) is the pointwise measurement of the plate displacement and x_ℓ, $\ell = 1, \cdots, N_s$, represent the locations of the sensors (accelerometers), with N_s the number of sensors. Finally, $\|\varphi\| = \sqrt{\varphi \cdot \overline{\varphi}}$ for vector $\varphi \in \mathbb{C}^2$ and $|v| = \sqrt{v\overline{v}}$ for scalar $v \in \mathbb{C}$ quantities, respectively, where $\overline{(\cdot)}$ represents the complex conjugate of $(\cdot)$.

Since we have no available experimental data, the measurement (w^*, θ^*) is obtained as the restriction at the points $x_\ell \in \Omega$, $\ell = 1, \cdots, N_s$, of the solution to (3.1) for $f(x) = f^*(x)$, where $f^* \in C_\delta(\Omega)$ is the south source defined as

$$f^*(x) = \sum_{i=1}^{N^*} \alpha_i^* \nabla_{x_i^*} \delta(x - x_i^*), \tag{3.8}$$

with the quantities N^*, x_i^* and α_i^* forming the set of unknowns characterizing the micro-faults to be reconstructed.

4. Sensitivity analysis

The next step is to minimize the misfit functional (3.7) in the set of admissible source densities (3.3). The idea is to perturb the trial source term $f \in C_\delta(\Omega)$ in (3.1) by a fixed number N of

additional point sources, namely

$$f_\delta(x) = f(x) + \sum_{i=1}^{N} \alpha_i \nabla_{x_i} \delta(x - x_i), \tag{4.1}$$

where $f_\delta \in C_\delta(\Omega)$ is the perturbed counterpart of the source term. On the basis of (3.1) and (4.1), we can introduce the forward solution $(\theta_\delta, w_\delta)$ as that solving: Find $(\theta_\delta, w_\delta)$, such that

$$\left\{ \begin{array}{rcl} -\mathrm{div}\mathcal{M}(\theta_\delta) + \mathcal{Q}(\theta_\delta, w_\delta) - k_b^2 \theta_\delta &=& f_\delta, \\ \mathrm{div}\mathcal{Q}(\theta_\delta, w_\delta) - k_s^2 w_\delta &=& 0, \end{array} \right. \tag{4.2}$$

endowed with the essential boundary condition $w_\delta = 0$ on $\partial\Omega$. The associated perturbed counterpart of the cost functional is then given by

$$\mathcal{J}(w_\delta, \theta_\delta) = \frac{1}{2} \sum_{\ell=1}^{N_s} \int_\Omega (|w_\delta - w^*|^2 + \|\theta_\delta - \theta^*\|^2) \delta(x - x_\ell)\, dx. \tag{4.3}$$

Let us decompose the component α_i into its real and imaginary parts as

$$\alpha_i = a_i + \boldsymbol{i} b_i, \tag{4.4}$$

with $\boldsymbol{i} = \sqrt{-1}$ and $a_i, b_i \in \mathbb{R}$. Equations (4.1) and (4.4) induce the following ansätze for the solution $(\theta_\delta, w_\delta)$ to the system (4.2)

$$\theta_\delta(x) = \theta(x) + \sum_{i=1}^{N} (a_i + \boldsymbol{i} b_i) \theta_i(x), \tag{4.5}$$

for the rotation vector displacement field and

$$w_\delta(x) = w(x) + \sum_{i=1}^{N} (a_i + \boldsymbol{i} b_i) w_i(x), \tag{4.6}$$

for the transverse displacement field. After replacing (4.5) and (4.6) into (4.2), the following set of canonical problems can be identified: Find (θ_i, w_i), such that

$$\left\{ \begin{array}{rcl} -\mathrm{div}\mathcal{M}(\theta_i) + \mathcal{Q}(\theta_i, w_i) - k_b^2 \theta_i &=& \nabla_{x_i} \delta(x - x_i), \\ \mathrm{div}\mathcal{Q}(\theta_i, w_i) - k_s^2 w_i &=& 0, \end{array} \right. \tag{4.7}$$

endowed with the essential boundary condition $w_i = 0$ on $\partial\Omega$.

Here it is useful to note that canonical problems (4.7) are independent of the components a_i and b_i. By replacing (4.5) and (4.6) in (4.3), we obtain

$$\mathcal{J}(w_\delta,\theta_\delta)=\mathcal{J}(w,\theta)+\sum_{\ell=1}^{N_s}\int_\Omega\sum_{i=1}^{N}a_i(\Re\{w-w^*\}w_i+\Re\{\theta-\theta^*\}\cdot\theta_i)\delta(x-x_\ell)\,dx$$
$$+\sum_{\ell=1}^{N_s}\int_\Omega\sum_{i=1}^{N}b_i(\Im\{w-w^*\}w_i+\Im\{\theta-\theta^*\}\cdot\theta_i)\delta(x-x_\ell)\,dx$$
$$+\frac{1}{2}\sum_{\ell=1}^{N_s}\int_\Omega\sum_{i=1}^{N}\sum_{j=1}^{N}a_ia_j(w_iw_j+\theta_i\cdot\theta_j)\delta(x-x_\ell)\,dx$$
$$+\frac{1}{2}\sum_{\ell=1}^{N_s}\int_\Omega\sum_{i=1}^{N}\sum_{j=1}^{N}b_ib_j(w_iw_j+\theta_i\cdot\theta_j)\delta(x-x_\ell)\,dx. \tag{4.8}$$

For a systematic treatment of (4.8), we next introduce the vectors

$$a=(a_1,a_2,\cdots,a_N)^\top\in\mathbb{R}^N, \tag{4.9}$$
$$b=(b_1,b_2,\cdots,b_N)^\top\in\mathbb{R}^N, \tag{4.10}$$

With such definitions, the expansion in (4.8) can be rewritten more compactly as

$$\Psi_N(a,b)=\mathcal{J}(w_\delta,\theta_\delta)-\mathcal{J}(w,\theta)$$
$$=p\cdot a+q\cdot b+\frac{1}{2}Ha\cdot a+\frac{1}{2}Hb\cdot b. \tag{4.11}$$

Here, the vectors $p,q\in\mathbb{R}^N$ and matrix $H\in\mathbb{R}^N\times\mathbb{R}^N$ are respectively defined as

$$p=\begin{pmatrix}p_1\\p_2\\\vdots\\p_N\end{pmatrix},\quad q=\begin{pmatrix}q_1\\q_2\\\vdots\\q_N\end{pmatrix}\quad\text{and}\quad H=\begin{pmatrix}H_{11}&H_{12}&\dots&H_{1N}\\H_{21}&H_{22}&\dots&H_{2N}\\\vdots&\vdots&\ddots&\vdots\\H_{N1}&H_{N2}&\dots&H_{NN}\end{pmatrix}, \tag{4.12}$$

whose entries are given by

$$p_i=\sum_{\ell=1}^{N_s}\int_\Omega(\Re\{w-w^*\}w_i+\Re\{\theta-\theta^*\}\cdot\theta_i)\delta(x-x_\ell)\,dx, \tag{4.13}$$
$$q_i=\sum_{\ell=1}^{N_s}\int_\Omega(\Im\{w-w^*\}w_i+\Im\{\theta-\theta^*\}\cdot\theta_i)\delta(x-x_\ell)\,dx, \tag{4.14}$$

and

$$H_{ij}=\sum_{\ell=1}^{N_s}\int_\Omega(w_iw_j+\theta_i\cdot\theta_j)\delta(x-x_\ell)\,dx. \tag{4.15}$$

5. Reconstruction algorithm

Let us define the vector of trial source locations as

$$\eta=(x_1,x_2,\cdots,x_N)\in\mathbb{R}^N. \tag{5.1}$$

By applying the first-order optimality condition to the quadratic form Ψ_N with respect to a and b, we obtain

$$D_a\Psi_N(a,b)\cdot\delta a=0,\quad\forall\delta a\in\mathbb{R}^N, \tag{5.2}$$
$$D_b\Psi_N(a,b)\cdot\delta b=0,\quad\forall\delta b\in\mathbb{R}^N. \tag{5.3}$$

This leads to the following linear systems

$$Ha = -p \quad \text{and} \quad Hb = -q. \tag{5.4}$$

Note that we have $a = a(\eta)$ and $b = b(\eta)$ because of the implicit dependence between the solutions of the linear systems (5.4) with (5.1). Furthermore, after replacing (5.4) into (4.11), the vector of optimal locations $\eta^\star$ can be obtained as solution to the following minimization problem:

$$\eta^\star = \underset{\eta \subset X}{\operatorname{argmin}} \left\{ \Psi_N(a(\eta), b(\eta)) = \frac{1}{2}(p \cdot a(\eta) + q \cdot b(\eta)) \right\}, \tag{5.5}$$

with X used to denote the set of trial sources localization. Finally, the optimal moment tensor components are given by $a^\star = a(\eta^\star)$ and $b^\star = b(\eta^\star)$.

The resulting second order reconstruction algorithm is now introduced. Its entries are given by the number of point sources N, the grid forming the set of source locations X and the vectors p, q and the matrix H. The algorithm returns the optimal set of source localization $\eta^\star$ and the respective moment tensor components $(a^\star, b^\star)$, together with the optimal value of the objective functional $\Psi_N^\star$. The above procedure is conveniently presented in a pseudo-code format through Algorithm 1. Therein, Π maps the vector of source indices $\mathcal{I} = (i_1, i_2, \cdots, i_N)$ to the corresponding vector of source locations $\eta \subset X$.

Algorithm 1: Micro-seismic fault reconstruction

input : N, X, H, p, q;
output: the optimal solution $\eta^\star$, $(a^\star, b^\star)$, $\Psi_N^\star$;
initialization: $\eta^\star \leftarrow 0$, $(a^\star, b^\star) \leftarrow (0, 0)$, $\Psi_N^\star \leftarrow \infty$;
for $i_1 \leftarrow 1$ to card$\{X\}$ do
  for $i_2 \leftarrow i_1 + 1$ to card$\{X\}$ do
    $\vdots$
    for $i_N \leftarrow i_{N-1} + 1$ to card$\{X\}$ do

$$p \leftarrow \begin{pmatrix} p_{(i_1)} \\ p_{(i_2)} \\ \vdots \\ p_{(i_N)} \end{pmatrix}, \; q \leftarrow \begin{pmatrix} q_{(i_1)} \\ q_{(i_2)} \\ \vdots \\ q_{(i_N)} \end{pmatrix}, \; H \leftarrow \begin{pmatrix} H_{(i_1,i_1)} & H_{(i_1,i_2)} & \cdots & H_{(i_1,i_N)} \\ H_{(i_2,i_1)} & H_{(i_2,i_2)} & \cdots & H_{(i_2,i_N)} \\ \vdots & \vdots & \ddots & \vdots \\ H_{(i_N,i_1)} & H_{(i_N,i_2)} & \cdots & H_{(i_N,i_N)} \end{pmatrix};$$

      $a \leftarrow -H^{-1}p$, $b \leftarrow -H^{-1}q$, $\Psi_N \leftarrow \frac{1}{2}(p \cdot a + q \cdot b)$;
      $\mathcal{I} \leftarrow (i_1, i_2, \cdots, i_N)$, $\eta \leftarrow \Pi(\mathcal{I})$;
      if $\Psi_N < \Psi_N^\star$ then
        $\eta^\star \leftarrow \eta$, $(a^\star, b^\star) \leftarrow (a, b)$, $\Psi_N^\star \leftarrow \Psi_N$;
      end if
    end for
  end for
end for

6. Numerical results

In this section, we present some numerical experiments. We consider a simply supported square-shaped plate of dimensions $\Omega = (0, 1) \times (0, 1)\,\mathrm{m}^2$ and thickness $h = 10^{-2}\mathrm{m}$ ($1\,\mathrm{cm}$). The area a_Ξ and the jump $[\![w]\!]$ of the micro-fault are of order $10^{-4}\mathrm{m}^2$ ($1\,\mathrm{cm}^2$) and $10^{-3}\mathrm{m}$ ($1\,\mathrm{mm}$), respectively, which will be specified later on according to the experiment we are dealing with.

The frequency of wave motion $\omega = 2\pi \times 200\,\text{rad/s}$. The physical material properties of the plate made with steel are Young Modulus $E = 210\,\text{GPa}$, Poisson ratio $\nu = 0.3$ and density $\rho = 7800\,\text{kg/m}^3$. The parameter $\alpha_i \in \mathbb{C}$ from (3.3) is the complex valued fault apertures, with $i = 1, \cdots, N$. The direct (3.1) and canonical (4.7) problems are solved numerically by using the Finite Element Method according to [42]. Specifically, the square-shaped plate is split into 100 uniform squares. Thus, each smaller square is divided into 4 identical triangles. The set of admissible source locations X is formed by the resulting vertices after disregarding the ones over the boundary, leading to $\text{card}\{X\} = 181$. In order to fulfill the Ihlenburg-Babuška condition [43], each triangle is divided into 4 more triangles in such a way that the initial pattern is preserved. This procedure is repeated two times, leading to 6400 triangles. The resulting mesh is then used to discretize the boundary value problems. The proposed method was coded in MATLAB [44]. The numerical experiments were performed in a Windows machine endowed with dual Intel Core i5 10210U processor with a clock frequency of 1.60GHz, having 4 cores and 8GB of RAM.

The true (target) and the reconstructed micro-faults are represented graphically by blue and red circles, respectively. The radii of such circles are proportional to the associated micro-faults amplitudes. In all the numerical experiments to be presented, we consider the reconstruction of four simultaneous faults by using varying configurations of sensors. The locations $x_i^* \in X$ and fault apertures α_i^* to be reconstructed are summarised in Table 1.

TABLE 1. Parameters associated with the four anomalies to be reconstructed.

i	x_i^*	α_i^* $(\times 10^4)$
1	$(0.7, 0.6)$	$0.6923 + 0.6923\boldsymbol{i}$
2	$(0.3, 0.4)$	$0.6923 + 1.3846\boldsymbol{i}$
3	$(0.6, 0.2)$	$1.3846 + 0.6923\boldsymbol{i}$
4	$(0.2, 0.7)$	$1.3846 + 1.3846\boldsymbol{i}$

The elapsed time need for solving the auxiliary problems is 4.1 seconds, whereas the reconstruction Algorithm 1 expend 260.7 seconds for $N = 4$ trial sources, which represents the main time consuming of the proposed approach, as expected. For a detailed discussion on the complexity of Algorithm 1, the reader may refer to [45].

6.1. **Example 1.** Different external factors may generate significant changes in the dynamic response of the pointwise sensors used to measure (w^*, θ^*) at $x_\ell \in \Omega$, with $\ell = 1, \cdots, N_s$, such as acoustic noise, temperature variations and humidity. Therefore, the measurement (w^*, θ^*) is corrupted with White Gaussian Noise (WGN) of varying levels, so that the noise represents uncertainties in the device measuring the displacement field. In all cases, the level of noise is fixed just below to the threshold for which the reconstruction becomes completely degraded, leading to spurious results.

We start by considering four three-axial pointwise sensors distributed along the boundary of the plate as shown in Figure 2. In this case, since the plate is simply supported, we have 8 degrees of freedom as available data. The results are presented in Figures 3 and 4 for 0% and 23% of WGN, respectively. For completeness, we present the values of $\alpha_i^\star$ obtained for 0% and 23% of WGN as detailed in Table 2.

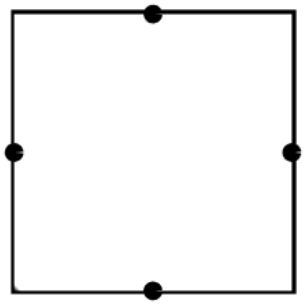

FIGURE 2. Example 1: Four three-axial sensors ($N_s = 4$) distributed on the boundary $\partial\Omega$ of the plate Ω, which are represented by black dots.

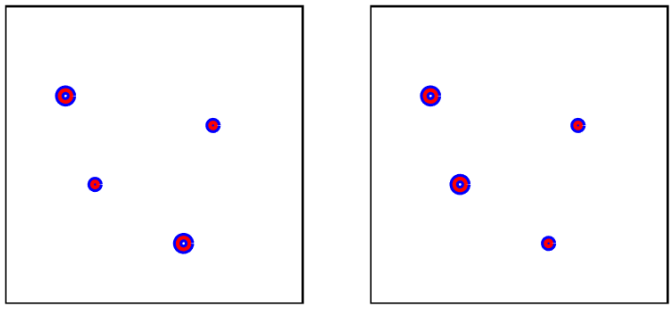

(a) real part (b) imaginary part

FIGURE 3. Example 1: Obtained result free of noise by considering four three-axial sensors as in Figure 2. The target and the reconstructed micro-faults are represented by blue and red circles, respectively. The radii of such circles are proportional to the associated micro-faults amplitudes.

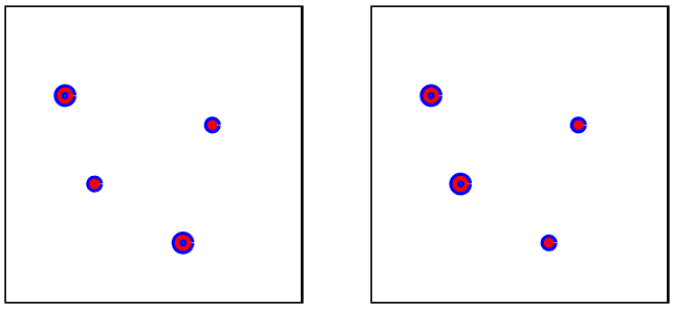

(a) real part (b) imaginary part

FIGURE 4. Example 1: Obtained result with 23% of WGN by considering four three-axial sensors as in Figure 2. The target and the reconstructed micro-faults are represented by blue and red circles, respectively. The radii of such circles are proportional to the associated micro-faults amplitudes.

TABLE 2. Example 1: Reconstructed values $\alpha_i^\star$ ($\times 10^4$) for 0% and 23% of WGN by considering four three-axial sensors as in Figure 2.

i	0% of WGN	23% of WGN
1	$0.6923 + 0.6923\boldsymbol{i}$	$0.6968 + 0.6830\boldsymbol{i}$
2	$0.6923 + 1.3846\boldsymbol{i}$	$0.6592 + 1.3733\boldsymbol{i}$
3	$1.3846 + 0.6923\boldsymbol{i}$	$1.3867 + 0.6933\boldsymbol{i}$
4	$1.3846 + 1.3846\boldsymbol{i}$	$1.3710 + 1.3729\boldsymbol{i}$

Now, we consider again four three-axial pointwise sensors, but localized within the plate as shown in Figure 5. In this case we have 12 degrees of freedom as available data. The results are presented in Figures 6 and 7 for 0% and 76% of WGN, respectively. The values of $\alpha_i^\star$ obtained for 0% and 76% of WGN are reported in Table 3.

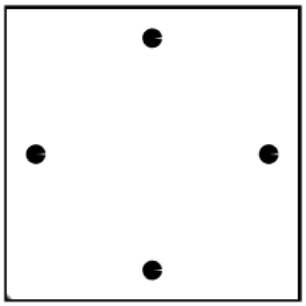

FIGURE 5. Example 1: Four three-axial sensors ($N_s = 4$) distributed on the boundary $\partial\Omega$ of the plate Ω, which are represented by black dots.

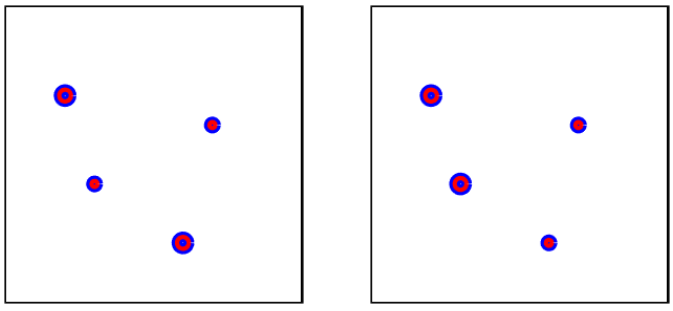

(a) real part (b) imaginary part

FIGURE 6. Example 1: Obtained result free of noise by considering four three-axial sensors as in Figure 5. The target and the reconstructed micro-faults are represented by blue and red circles, respectively. The radii of such circles are proportional to the associated micro-faults amplitudes.

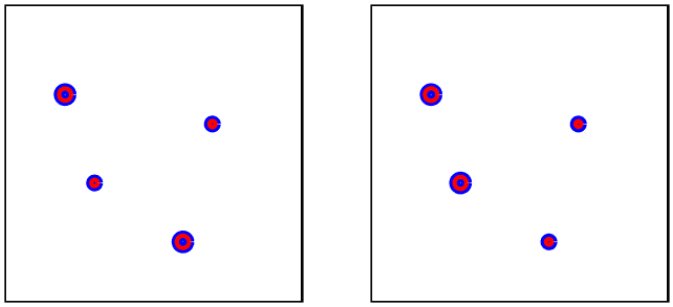

(a) real part (b) imaginary part

FIGURE 7. Example 1: Obtained result with 76% of WGN by considering four three-axial sensors as in Figure 5. The target and the reconstructed micro-faults are represented by blue and red circles, respectively. The radii of such circles are proportional to the associated micro-faults amplitudes.

TABLE 3. Example 1: Reconstructed values $\alpha_i^\star$ ($\times 10^4$) for 0% and 76% of WGN by considering four three-axial sensors as in Figure 5.

i	0% of WGN	76% of WGN
1	$0.6923 + 0.6923\boldsymbol{i}$	$0.7145 + 0.7493\boldsymbol{i}$
2	$0.6923 + 1.3846\boldsymbol{i}$	$0.7613 + 1.2260\boldsymbol{i}$
3	$1.3846 + 0.6923\boldsymbol{i}$	$1.4598 + 0.5927\boldsymbol{i}$
4	$1.3846 + 1.3846\boldsymbol{i}$	$1.3703 + 1.4478\boldsymbol{i}$

Finally, we consider eight three-axial pontwise sensors as shown is Figure 8, where four sensors are localized on the boundary and four into the plate. Therefore, in this case we have 20 degrees of freedom as available data. The results are presented in Figures 9 and 10 with 0% and 86% of WGN, respectively. In Table 4 we present the values obtained for $\alpha_i^\star$ with 0% and 86% of WGN.

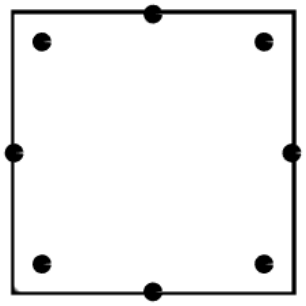

FIGURE 8. Example 1: Eight three-axial sensors ($N_s = 8$) distributed on the boundary $\partial\Omega$ of the plate Ω, which are represented by black dots.

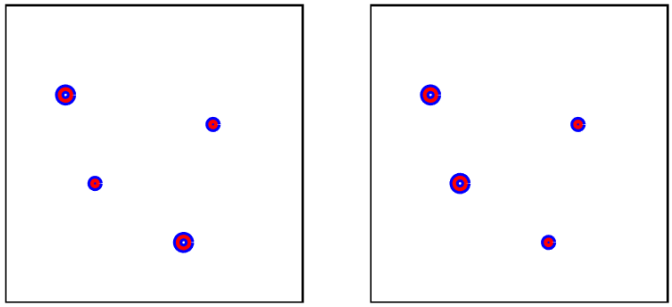

(a) real part (b) imaginary part

FIGURE 9. Example 1: Obtained result free of noise by considering eight three-axial sensors as in Figure 8. The target and the reconstructed micro-faults are represented by blue and red circles, respectively. The radii of such circles are proportional to the associated micro-faults amplitudes.

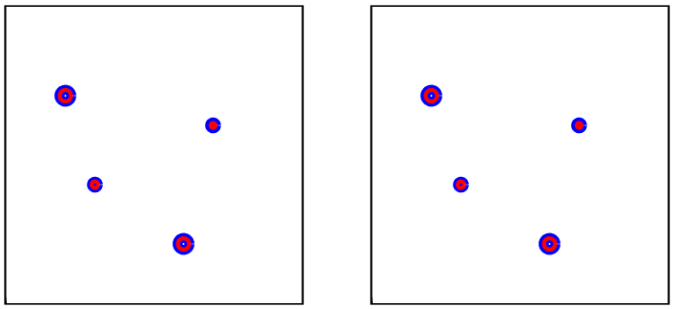

(a) real part (b) imaginary part

FIGURE 10. Example 1: Obtained result with 86% of WGN by considering eight three-axial sensors as in Figure 8. The target and the reconstructed micro-faults are represented by blue and red circles, respectively. The radii of such circles are proportional to the associated micro-faults amplitudes.

TABLE 4. Example 1: Reconstructed values $\alpha_i^\star$ ($\times 10^4$) for 0% and 86% of WGN by considering eight three-axial sensors as in Figure 8.

i	0% of WGN	86% of WGN
1	$0.6923 + 0.6923\boldsymbol{i}$	$0.6931 + 0.6190\boldsymbol{i}$
2	$0.6923 + 1.3846\boldsymbol{i}$	$0.5922 + 1.4125\boldsymbol{i}$
3	$1.3846 + 0.6923\boldsymbol{i}$	$1.2818 + 0.7268\boldsymbol{i}$
4	$1.3846 + 1.3846\boldsymbol{i}$	$1.3355 + 1.2671\boldsymbol{i}$

6.2. **Example 2.** In this example, the material properties from the background are corrupted with White Gaussian Noise. More precisely, the corrupted material parameters are computed in the finite element mesh used to generate the set X, with 400 triangles. For consistency, such material distribution is then projected onto a finer mesh with 6400 triangular elements used to solve the boundary value problems. Therefore, in this case, the noisy represents random modeling uncertainties. For completeness, the noisy data is plotted in Figure 11. As in the former

example, the level of noise is fixed just below to the threshold for which the reconstruction becomes completely degraded, leading to spurious results.

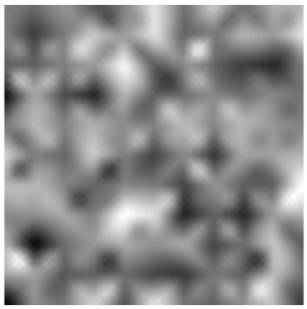

FIGURE 11. Example 2: Young modulus distribution within the plate Ω corrupted with White Gaussian Noise.

In the first case, we aim to reconstruct four simultaneous faults using four three-axial pointwise sensors as shown in Figure 2. The result is presented in Figure 12 for 20% of WGN. In Table 5, the values obtained for $\alpha_i^\star$ with 20% of WGN are presented.

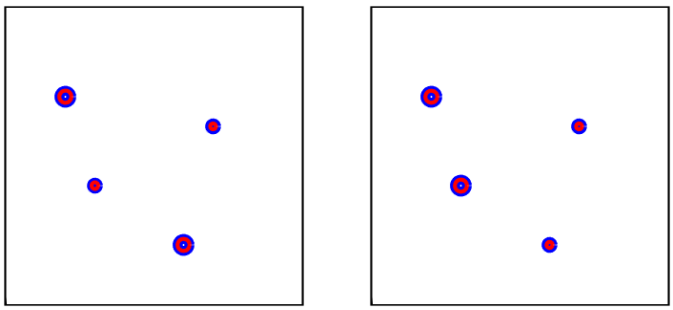

(a) real part (b) imaginary part

FIGURE 12. Example 2: Obtained result with 20% of WGN by considering four three-axial sensors as in Figure 2. The target and the reconstructed micro-faults are represented by blue and red circles, respectively. The radii of such circles are proportional to the associated micro-faults amplitudes.

TABLE 5. Example 2: Reconstructed values $\alpha_i^\star$ ($\times 10^4$) for 20% of WGN by considering four three-axial sensors as in Figure 2.

i	20% of WGN
1	$0.6927 + 0.6615\boldsymbol{i}$
2	$0.7017 + 1.4379\boldsymbol{i}$
3	$1.3633 + 0.7152\boldsymbol{i}$
4	$1.4037 + 1.3815\boldsymbol{i}$

Now, we reconstruct four faults using four three-axial pointwise sensors as shown in Figure 5. The result is presented in Figure 13 for 49% of WGN. In Table 6, we present the values obtained for $\alpha_i^\star$ with 49% of WGN.

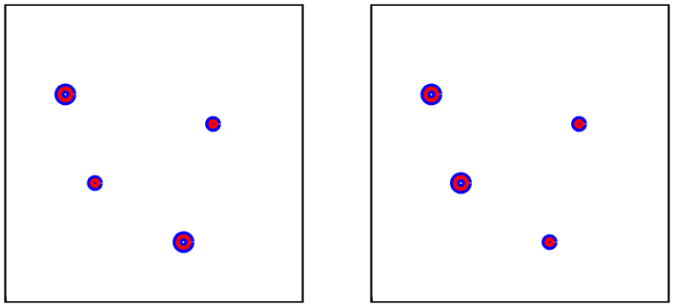

(a) real part (b) imaginary part

FIGURE 13. Example 2: Obtained result with 49% of WGN by considering four three-axial sensors as in Figure 5. The target and the reconstructed micro-faults are represented by blue and red circles, respectively. The radii of such circles are proportional to the associated micro-faults amplitudes.

TABLE 6. Example 2: Reconstructed values $\alpha_i^\star$ ($\times 10^4$) for 49% of WGN by considering four three-axial sensors as in Figure 5.

i	49% of WGN
1	$0.6640 + 0.7393\boldsymbol{i}$
2	$0.6599 + 1.4635\boldsymbol{i}$
3	$1.3583 + 0.6519\boldsymbol{i}$
4	$1.4001 + 1.3756\boldsymbol{i}$

Finally, we consider eight three-axial pointwise sensors as shown in Figure 8. The result is presented in Figure 14 for 69% of WGN. In Table 7, the values obtained for $\alpha_i^\star$ with 69% of WGN are reported.

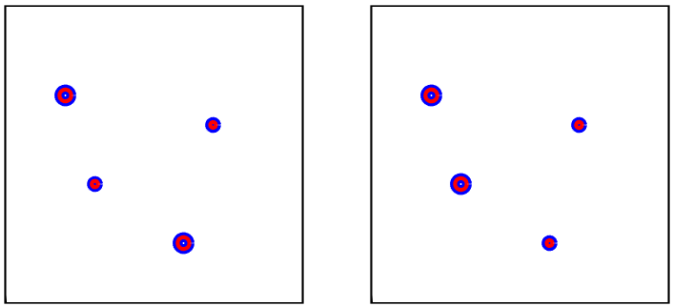

(a) real part (b) imaginary part

FIGURE 14. Example 2: Obtained result with 69% of WGN by considering eight three-axial sensors as in Figure 8. The target and the reconstructed micro-faults are represented by blue and red circles, respectively. The radii of such circles are proportional to the associated micro-faults amplitudes.

TABLE 7. Example 2: Reconstructed values $\alpha_i^\star$ ($\times 10^4$) for 69% of WGN by considering eight three-axial sensors as in Figure 8.

i	69% of WGN
1	$0.6287 + 0.8050\boldsymbol{i}$
2	$0.5915 + 1.5674\boldsymbol{i}$
3	$1.3069 + 0.6896\boldsymbol{i}$
4	$1.3383 + 1.4889\boldsymbol{i}$

6.3. **Example 3.** In this third example, we consider twenty four uni-axial sensors as shown in Figure 15, in which only the transverse degree of freedom is available. As in the fist example, the measurements are corrupted with White Gaussian Noise (WGN). The reconstruction for 0% of WGN is exact, as expected. The results for 48% of WGN are presented in Figures 16, which fit quite well the target even in the presence of such a high level of noise. The reconstruction for 49% of WGN or higher becomes completely degraded, leading to spurious results.

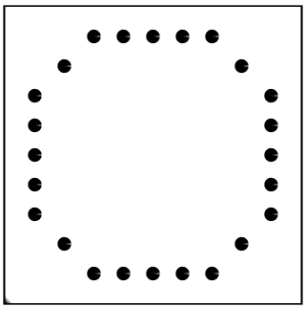

FIGURE 15. Example 3: Twenty four uni-axial sensors ($N_s = 24$) distributed on the boundary $\partial\Omega$ of the plate Ω, which are represented by black dots.

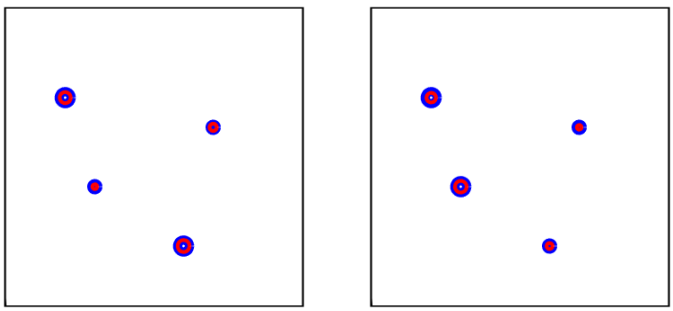

(a) real part (b) imaginary part

FIGURE 16. Example 3: Obtained results for 48% of WGN by considering twenty four uni-axial sensors as in Figure 15. The target and the reconstructed micro-faults are represented by blue and red circles, respectively. The radii of such circles are proportional to the associated micro-faults amplitudes.

7. CONCLUSIONS

In this paper, a new micro-seismic fault reconstruction method in Reissner-Mindlin plates model has been proposed. The micro-seismic faults are modeled by a combination of dipoles written in terms of the seismic moment tensor. A functional measuring the misfit between

observed and predicted data has been minimized with respect to a set of admissible micro-seismic sources by using the topological derivative method. The obtained theoretical result has been used to devise a non-iterative and initial-guess free second order reconstruction algorithm proved to be very resilient with respect to noisy data. In fact, a set of numerical experiments dealing with the reconstruction of four simultaneous faults has been presented by considering varying configurations of three as well as uni-axial pointwise sensors in the presence and absence of noisy data. In particular, either the measurements or the material properties of the background have been corrupted with White Gaussian Noise (WGN) of varying levels. In Examples 1 and 2 we have considered different configurations of three-axial pointwise sensors. On the other hand, in Example 3 a set of uni-axial pointwise sensors has been considered, in which only the transverse degree of freedom is assumed to be available. In all cases, the reconstructions were shown to be exact (up to a small numerical threshold) in the absence of noise and of good quality even in the presence of high level of noise. Therefore, the main contributions of the paper consist of two folds. The first one is related to the micro-seismic faults modeling in plate structures itself. More precisely, the model problem (3.1) is new, so that up to now there is no any available theoretical results to compare with our finds. On the other hand, it has been rigorously derived from a well-established theory posed into three spatial dimensions fully developed in the book by Aki and Richards [40], which has been particularized to the kinematic assumptions of Reissner-Mindlin plates. The second one consists in the micro-seismic faults reconstruction Algorithm 1 from pointwise measurements of the plate displacement field, which can naturally be used for monitoring sudden appearance of small faults in plate structures. However, in the proposed model we have considered micro-faults lying in the middle plane of the plate under opening mechanism in traction, only. Therefore, further developments are necessary to deal with more realistic scenario, including opening mechanisms in shear mode and micro-seismic fault reconstruction in layered plates, for instance. These extensions will be subject of future research.

Acknowledgements

This research was partly supported by CNPq (Brazilian Research Council), CAPES (Brazilian Higher Education Staff Training Agency) and FAPERJ (Research Foundation of the State of Rio de Janeiro). These financial support are gratefully acknowledged. We would like to thanks Professor Bojan Guzina for many fruitful discussions.

References

[1] G. Gomes, S. da Cunha Jr, and A. Jr, "A sunflower optimization (sfo) algorithm applied to damage identification on laminated composite plates," *Engineering with Computers*, 2018.

[2] J. Lee, J. W. Lee, J. Yi, C. Yun, and H. Jung, "Neural networks-based damage detection for bridges considering errors in baseline finite element models," *Journal of Sound and Vibration*, vol. 280, pp. 555–578, 2005.

[3] U. Lee and J. Shin, "A structural damage identification method for plate structures," *Engineering Structures*, vol. 24, pp. 1177–1188, 2002.

[4] A. Pandey and M. Biswas, "Damage detection in structures using changes in flexibility," *Journal and Sound and Vibration*, vol. 169, pp. 3–17, 1994.

[5] A. Pandey, M. Biswas, and M. Samman, "Damage detection from changes in curvature mode shapes," *Journal and Sound and Vibration*, vol. 145, pp. 321–332, 1991.

[6] M. Rao, J. Srinivas, and B. Murthy, "Damage detection in vibrating bodies using genetic algorithms," *Computers and Structures*, vol. 82, pp. 963—968, 2004.

[7] O. Salawu and C. Williams, "Bridge assessment using forced-vibration testing," *Journal of Structural Engineering*, vol. 121, pp. 161–173, 1995.

[8] S. Sandesh and K. Shankarb, "Damage identification of a thin plate in the time domain with substructuring-an application of inverse problem," *International Journal of Applied Science and Engineering*, vol. 7, pp. 79–93, 2009.
[9] J. Santos, C. Soares, C. Soares, and H. Pina, "Development of a numerical model for the damage identification on composite plate structures," *Composite Structures*, vol. 48, pp. 59–65, 2000.
[10] L. Stutz, D. Castello, and F. Rochinha, "A flexibility-based continuum damage identification approach," *Journal of Sound and Vibration*, vol. 279, pp. 641–667, 2005.
[11] L. Stutz, R. Tenenbaum, and R. Corrêa, "The differential evolution method applied to continuum damage identification via flexibility matrix," *Journal of Sound and Vibration*, vol. 345, pp. 86–102, 2015.
[12] R. Tenenbaum, L. Stutz, and K. Fernandes, "Damage identification in bars with a wave propagation approach: Performance comparison of five hybrid optimization methods," *Shock and Vibration*, vol. 20, pp. 863–878, 2013.
[13] A. Tomaszewska, "Influence of statistical errors on damage detection based on structural flexibility and mode shape curvature," *Computers and Structures*, vol. 88, pp. 154–164, 2010.
[14] Y. Xia and H. Hao, "Statistical damage identification of structures with frequency changes," *Journal of Sound and Vibration*, vol. 263, pp. 853–870, 2003.
[15] A. Rytter, *Vibrational Based Inspection of Civil Engineering Structures*. Ph.D. Thesis, Dept. of Building Technology and Structural Engineering, Aalborg University, Denmark, 1993.
[16] A. A. M. Silva and A. A. Novotny, "Damage identification in plate structures based on the topological derivative method," *Structural and Multidisciplinary Optimization*, vol. 65, 2022.
[17] A. A. S. Amad, A. A. Novotny, and B. Guzina, "On the full-waveform inversion of seismic moment tensors," *International Journal of Solids and Structures*, vol. 202, no. 1, pp. 717–728, 2020.
[18] A. A. Novotny and J. Sokołowski, *Topological derivatives in shape optimization*. Interaction of Mechanics and Mathematics, Berlin, Heidelberg: Springer-Verlag, 2013.
[19] A. Schumacher, *Topologieoptimierung von bauteilstrukturen unter verwendung von lochpositionierungkriterien*. Ph.D. Thesis, Universität-Gesamthochschule-Siegen, Siegen - Germany, 1995.
[20] J. Sokołowski and A. Żochowski, "On the topological derivative in shape optimization," *SIAM Journal on Control and Optimization*, vol. 37, no. 4, pp. 1251–1272, 1999.
[21] S. Garreau, P. Guillaume, and M. Masmoudi, "The topological asymptotic for PDE systems: the elasticity case," *SIAM Journal on Control and Optimization*, vol. 39, no. 6, pp. 1756–1778, 2001.
[22] A. A. Novotny, S. M. Giusti, and S. Amstutz, "Guest Editorial: On the topological derivative method and its applications in computational engineering," *Engineering Computations*, vol. 39, no. 1, pp. 1–2, 2022.
[23] S. Amstutz, "An introduction to the topological derivative," *Engineering Computations*, vol. 39, no. 1, pp. 3–33, 2022.
[24] P. Baumann and K. Sturm, "Adjoint-based methods to compute higher-order topological derivatives with an application to elasticity," *Engineering Computations*, vol. 39, no. 1, pp. 60–114, 2022.
[25] M. Delfour, "Topological derivatives via one-sided derivative of parametrized minima and minimax," *Engineering Computations*, vol. 39, no. 1, pp. 34–59, 2022.
[26] P. Kliewe, A. Laurain, and K. Schmidt, "Shape optimization in acoustic-structure interaction," *Engineering Computations*, vol. 39, no. 1, pp. 172–200, 2022.
[27] A. Romero, "Optimum design of two-material bending plate compliant devices," *Engineering Computations*, vol. 39, no. 1, pp. 395–420, 2022.
[28] R. Santos and C. Lopes, "Topology optimization of structures subject to self-weight loading under stress constraints," *Engineering Computations*, vol. 39, no. 1, pp. 380–394, 2022.
[29] M. Bonnet, "On the justification of topological derivative for wave-based qualitative imaging of finite-sized defects in bounded media," *Engineering Computations*, vol. 39, no. 1, pp. 313–336, 2022.
[30] A. Canelas and J. Roche, "Shape and topology optimal design problems in electromagnetic casting," *Engineering Computations*, vol. 39, no. 1, pp. 147–171, 2022.
[31] L. Fernandez and R. Prakash, "Imaging of small penetrable obstacles based on the topological derivative method," *Engineering Computations*, vol. 39, no. 1, pp. 201–231, 2022.
[32] F. L. Louër and M. Rapún, "Topological sensitivity analysis revisited for time-harmonic wave scattering problems. Part I: The free space case," *Engineering Computations*, vol. 39, no. 1, pp. 232–271, 2022.
[33] F. L. Louër and M. Rapún, "Topological sensitivity analysis revisited for time-harmonic wave scattering problems. Part II: Recursive computations by the boundary integral equation method," *Engineering Computations*, vol. 39, no. 1, pp. 272–312, 2022.
[34] A. Ferrer and S. Giusti, "Inverse homogenization using the topological derivative," *Engineering Computations*, vol. 39, no. 1, pp. 337–353, 2022.

[35] R. Yera, L. Forzani, C. Méndez, and A. Huespe, "A topology optimization algorithm based on topological derivative and level-set function for designing phononic crystals," *Engineering Computations*, vol. 39, no. 1, pp. 354–379, 2022.
[36] M. Xavier and N. Van Goethem, "Brittle fracture on plates governed by topological derivatives," *Engineering Computations*, vol. 39, no. 1, pp. 421–437, 2022.
[37] L. Rakotondrainibe, G. Allaire, and P. Orval, "Topological sensitivity analysis with respect to a small idealized bolt," *Engineering Computations*, vol. 39, no. 1, pp. 115–146, 2022.
[38] G. Barros, J. Filho, L. Nunes, and M. Xavier, "Experimental validation of a topological derivative-based crack growth control method using digital image correlation," *Engineering Computations*, vol. 39, no. 1, pp. 438–454, 2022.
[39] P. Shearer, *Introduction to Seismology*. Cambridge University Press, 2009.
[40] K. Aki and P. Richards, *Quantitative Seismology*. Sausalito, California: University Science Books, 2009.
[41] F. Gilbert, "Derivation of source parameters from low-frequency spectra," *Philosophical Transactions of the Royal Society of London. Series A, Mathematical and Physical Sciences*, vol. 274, pp. 369–371, 1973.
[42] K. I., "A new discrete Kirchhof-Mindlin element based on Mindlin-Reissner plate theory and assumed shear strain fields—part i: An extended dkt element for thick-plate bending analysis," *International Journal for Numerical Methods in Engineering*, vol. 36, no. 11, pp. 1859–1883, 1993.
[43] F. Ihlenburg and I. Babuška, "Finite element solution of the Helmholtz equation with high wave number part i: The h-version of the FEM," *Computers & Mathematics with Applications*, vol. 30, no. 9, pp. 9–37, 1995.
[44] The MathWorks Inc., *MATLAB version: 9.13.0 (R2022b)*. Natick, Massachusetts, United States: The MathWorks Inc., 2022.
[45] T. J. Machado, J. S. Angelo, and A. A. Novotny, "A new one-shot pointwise source reconstruction method," *Mathematical Methods in the Applied Sciences*, vol. 40, no. 15, pp. 1367–1381, 2017.

Laboratório Nacional de Computação Científica LNCC/MCTI, Coordenação de Métodos Matemáticos e Computacionais, Av. Getúlio Vargas 333, 25651-075 Petrópolis - RJ, Brasil. These authors contributed equally to this work.

Email address: {andressa,novotny}@lncc.br